Will ultrathin CIGS solar cells overtake the champion thin-film cells? Updated SCAPS baseline models reveal main differences between ultrathin and standard CIGS

André F. Violas [a,b,c], António J.N. Oliveira [a,b,c], Jennifer P. Teixeira [a,*], Tomás S. Lopes [a,d,e,f], João R.S. Barbosa [a], Paulo A. Fernandes [a,b,g], Pedro M.P. Salomé [a,c]

[a] INL – International Iberian Nanotechnology Laboratory, Avenida Mestre José Veiga, Braga, 4715-330, Portugal
[b] i3N, Departamento de Física, Universidade de Aveiro, Campus Universitário de Santiago, Aveiro, 3810-193, Portugal
[c] Departamento de Física da Universidade de Aveiro, Campus Universitário de Santiago, Aveiro, 3810-193, Portugal
[d] Imec division IMOMEC (partner in Solliance), Wetenschapspark 1, Diepenbeek, 3590, Belgium
[e] Institute for Material Research (IMO), Hasselt University (partner in Solliance), Agoralaangebouw H, Diepenbeek, 3590, Belgium
[f] EnergyVille 2, Thor Park 8320, Genk, 3600, Belgium
[g] CIETI, Departamento de Física, Instituto Superior de Engenharia do Porto, Instituto Politécnico do Porto, Porto, 4200-072, Portugal

ARTICLE INFO

ABSTRACT

Cu(In,Ga)Se$_2$ (CIGS) solar cells are amongst the best performing thin-film technologies, with the latest performance gains being mainly due to recent years improvements obtained with post-deposition treatments (PDT). Moreover, thinning of the absorber layer down to sub-micrometre values (ultrathin absorbers) is of extreme importance for CIGS to be even more cost-effective and sustainable. However, electrical and optical limitations, such as rear interface recombination and insufficient light absorption, prevent the widespread implementation of ultrathin CIGS devices. The recent electrical CIGS simulation baseline models have failed to keep up with the experimental developments. Here an updated and experimentally based baseline model for electrical simulations in the Solar Cell Capacitor Simulator (SCAPS) software is presented and discussed with the incorporation of the PDT effects and increased optical accuracy with the support from Finite-Difference Time-Domain (FDTD) simulation results. Furthermore, a champion solar cell with an equivalent architecture validates the developed thin-film model. The baseline model is also applied to ultrathin CIGS solar cell devices, validated with the ultrathin champion cell. Ultimately, these ultrathin models pave the way for an ultrathin baseline model. Simulations results reveal that addressing these absorbers' inherent limitations makes it possible to achieve an ultrathin solar cell with at least 21.0% power conversion efficiency, with open-circuit voltage values even higher than the recent thin-film champion cells.

1. Introduction

Cu(In,Ga)Se$_2$ (CIGS) thin-film solar cells belong to one of the most efficient photovoltaic (PV) technologies [1], with a record of light to power conversion efficiency value of 23.35% [2], being comparable with poly-crystalline silicon (Si) solar cells, 24.4% [1]. To further improve the CIGS devices' performance, a deeper knowledge of the material and solar cell fundamental properties should be developed. Electrical simulations have constantly supported the discussion of critical improvement pathways and possible solar cell limitations. Literature numerical simulations studies [3–5], and others with additional

experimental results [6–10], are main directives in the research community. The Solar Cell Capacitor Simulator (SCAPS) one dimensional simulation software [11] is commonly and freely used for thin-film PV technology and at its core is specifically designed for CIGS and CdTe technologies. Therefore, this study uses SCAPS due to its simplicity compared to other multi-dimensional software and suitability for CIGS solar cells. A good way to understand a specific phenomenon with the support from simulation results is in line with the change of a small number of parameters based on predefined ones from the electrical model [12]. Consequently, baseline models are useful to discuss the properties and performance of champion CIGS solar cells. However, a

---

baseline model for CIGS solar cells is a complex task due to the material complexity in terms of defects. CIGS is a semiconductor compound with a p-type behavior governed by its native defect nature, mostly arising from the acceptor Cu vacancy (V_{Cu}) due to the combination of a shallow energetic transition level of ~ 0.03 eV above the valence band maximum (VBM) and a respective low formation energy [13–16]. Thus, CIGS is designated as a self-doped material. Other native point-type defect present in the solar cell are the antisite defects, such as In on Cu (In_{Cu}) and Cu on In (Cu_{In}) defects [17]. Moreover, the literature points to the existence of a Cu-poor phase at the CIGS front surface with a bandgap value higher than in the bulk region [18–20], where, dependent from the authors, such phase may have different designations, i.e. ordered vacancy or defect compound (OVC or ODC, respectively) [21]. Therefore, due to its complexity, the CIGS SCAPS baseline model was only updated twice in the past twenty years: by Gloeckler et al. [22] in 2003 and by Pettersson et al. [12] in 2011. Since 2011, several development events in CIGS technology helped to enhance the performance of CIGS solar cells, from 20.3% [23] to 23.35% [2]. The development of the post-deposition treatment (PDT) with heavy alkali fluoride compounds, such as KF [24], RbF [25], and CsF [26] led to the main referred CIGS performance improvement. Pettersson's CIGS baseline model did not include PDT effects, meaning that an updated baseline model with PDT is lacking in the CIGS community.

To further lower the fabrication costs and the material consumption in CIGS devices, as well as to increase the manufacturing throughput, researchers worldwide are undertaking efforts to develop ultrathin (~ 500 nm) CIGS solar cells [27,28]. However, some performance limitations hinder the full potential of ultrathin devices, such as insufficient light absorption [29–32] and rear interface recombination [33,34]. The first may be tackled with light management [29,31,35–38] schemes, whereas the latter may be addressed with passivation strategies [33,34, 36,39,40]. Thus, given the ultrathin CIGS solar cells challenges a baseline model will help understand the technology current limitations and pave the way for future improvement strategies.

This study develops an updated electrical baseline model that addresses the recent developments in CIGS technology. The literature data and in-house experimental results feed the thin-film model, being validated with a 22.6% efficient champion solar cell [25] which is the highest performing pure selenide CIGS solar cell. Moreover, the updated baseline model describes the beneficial effects of PDT, and it includes other CIGS features, as its native defects nature. Additionally, the 3D Finite-Difference Time-Domain (FDTD) optical simulations within the *Lumerical* package [41] support the SCAPS baseline results, by providing the rear and front contact reflection optical data. The thin-film baseline model for high-efficiency solar cells is extended for champion ultrathin devices, where a comparison with experimental data proves its reliability. Finally, some limitations of ultrathin solar cells are addressed, considering optical and electrical properties, namely rear and front reflection, and rear interface and bulk recombination, respectively. Therefore, this work also provides a pathway of a baseline model for ultrathin CIGS solar cells as well as it demonstrates the potential of ultrathin devices to outperform the traditional ones.

2. Baseline model for high-efficiency thin-film devices

The PDT advances in CIGS solar cells have not yet been considered in former baseline SCAPS models. This study considers the Pettersson's model [12] as a starting point to achieve an updated and experimentally based baseline model for thin-film high-efficiency devices. Moreover, the validation of SCAPS model for high-efficiency devices is achieved through the comparison of the champion solar cell figures of merit with the same architecture described in the model [25].

2.1. Starting point

The proposed model takes into account 5 main layers together with

the respective contacts at the rear and front sides. Fig. 1 shows the considered architecture for the proposed model: CIGS absorber, surface defect layer (SDL), CdS, $Zn_{1-x}Mg_xO$ (ZMO), and Al:ZnO (AZO). The ZMO layer matches the champion cell architecture considered for experimental validation [8,25]. The implementation of the SDL layer and two layers to describe the i-ZnO/AZO bilayer is not consensual in the literature, since some simulation studies may or may not include them [6,7, 22,42–44]. However, the implementation of an SDL and a i-ZnO/AZO bilayer represent more accurately experimental results [19,45,46] and real devices [25]. The existence of a SDL may be explained by a Cu-poor phase present at the CIGS surface near the p-n junction with an increased bandgap value than the one at the bulk [3,18,19,44,45,47]. Moreover, the role of SDL as a hole barrier leads to a decrease in the CIGS (/SDL)/CdS interface recombination probability [18,46,48,49]. Hence, the SDL layer was simulated as a 15 nm CIGS with a higher bandgap energy (1.42 eV for the SDL vs. 1.23 eV at the CIGS surface) and a lower carrier mobility value (10 times lower for the SDL than in CIGS) compared to the CIGS absorber layer. The transparent conductive oxide (TCO) layers have different light absorption properties beyond the expected difference in doping levels, hence, two distinguished layers should be considered.

The thickness of all the layers present in the solar cell stack was defined according to the experimental champion cells [25] with the same architecture. Note that the very thin CdS thickness value (21 nm), present in Fig. 1, results from the use of PDT, where the CdS growth at initial stages by chemical bath deposition is more homogeneous [2,7,26, 50]. Chirila et al. reported the feasibility of a 10 nm thinner CdS layer without electrical losses compared with their standard process owing to the use of PDT [50]. In Table 1, the parameters extracted from Pettersson's model and the updated ones are presented. Any other parameter not mentioned in this study follows the work from Pettersson et al. [12]. This study updates the absorption coefficient values for all layers. Hence, the CIGS optical constants are taken from the work performed by Fujiwara et al. [51,52], where they provide a complete database of the optical properties of CIGS absorber layers with different [Ga]/([Ga] + [In]) (GGI) values, allowing to simulate the gradient Ga-profile existent in high-efficiency solar cells. The CdS and AZO optical properties are based on the work from Carron et al. [53], where the absorption data for the AZO layer accounts for the free carriers' light absorption at the infrared (IR) wavelength range. Finally, the ZMO optical constant is based on Kumar et al. [54] considering a Mg content of 25% [8].

Thin-film high-efficiency devices with power conversion efficiency >20% are fabricated with a double bandgap grading scheme in the absorber layer. In common double Ga grading schemes, the rear surface has a high concentration of Ga, which decreases towards the front surface, until a minimum value -the so called notch- is reached, followed by an increase at the front surface [55]. Moreover, the intermixing of In by Ga increases the bandgap value and it mostly influences the CIGS conduction band minimum (CBM) [56]. Hence, a Ga-grading scheme promotes a preferential direction movement of the charge carriers. By
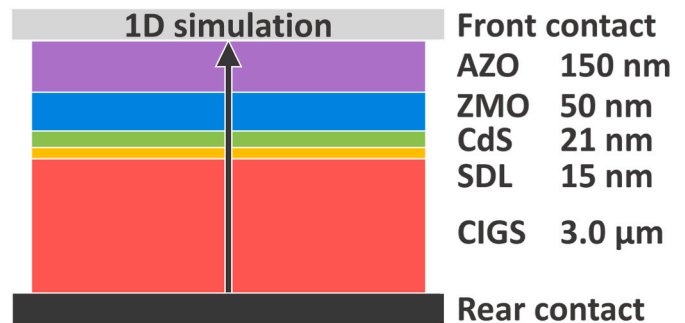

Fig. 1. SCAPS model schematic of the different layers. Thicknesses are not at scale.

Table 1

SCAPS parameters for the final baseline model of this study. The interface defects are used according to Pettersson's study [12]. The bulk defects are divided into double donor (1), double acceptor (2), and grain boundary GB (3) defects. Note that in the GB defects, the defect density is distributed in two halves for acceptor and donor single defects, i.e. single (A/D). "A" stands for acceptor, and "D" for donor. Whereas, E_g refers to the bandgap energy, ε_r to the relative dielectric function, N_C and N_V to the density of states at the CBM and at the VBM, respectively, v_{th}^e and v_{th}^h to the thermal velocity of electrons and holes, respectively, μ_e and μ_h to the mobility of electrons and holes, respectively, N_D and N_A to the shallow defect density for donors and acceptors, respectively, E_t and N_t to the defect energy level and density, respectively, and *SRV* to the surface recombination velocity. The SCAPS files may be provided upon request.

| Layer properties	CIGS	SDL	CdS	ZMO	AZO
Thickness (μm)	3.0	0.015 [12]	0.021	0.05	0.15
E_g (eV)	1.31–1.105 – 1.23 (Mo→notch→SDL)	1.42	2.4 [12]	3.8	3.3 [12]
χ_a (eV)	4.22–4.43–4.31 (Mo→notch→SDL)	4.31	4.11	4.21	4.21
ε_r	13.6 [12]	13.6 [12]	6.8	9 [12]	9 [12]
N_C (cm^{-3})	6.8×10^{17} [12]	6.8×10^{17} [12]	1.3×10^{18} [12]	3.0×10^{18} [12]	3.0×10^{18} [12]
N_V (cm^{-3})	1.5×10^{19} [12]	1.5×10^{19} [12]	9.1×10^{18} [12]	1.7×10^{19} [12]	1.7×10^{19} [12]
v_{th}^e (cm·s^{-1})	3.9×10^7 [12]	3.9×10^7 [12]	3.1×10^7 [12]	2.4×10^7 [12]	2.4×10^7 [12]
v_{th}^h (cm·s^{-1})	1.4×10^7 [12]	1.4×10^7 [12]	1.6×10^7 [12]	1.3×10^7 [12]	1.3×10^7 [12]
μ_e (cm^2·V^{-1}s^{-1})	100 [12]	10 [12]	72 [12]	100	100 [12]
μ_h (cm^2·V^{-1}s^{-1})	12.5 [12]	1.25 [12]	20 [12]	31 [12]	31 [12]
N_D (cm^{-3})	1.0×10^{16}	1.0×10^{16}	5.0×10^{17} [12]	1.0×10^{17} [12]	1.0×10^{20} [12]
N_A (cm^{-3})	6.0×10^{16}–1.1×10^{16} wo type-inv. (Mo → SDL)	1.1×10^{16} wo type-inv.	–	–	–
	6.0×10^{16}–1.0×10^{14} type-inv. (Mo → SDL)	1.0×10^{14} type-inv.			
α (cm^{-1})	[51,52]	[51,52]	[53]	[54]	[53]
Bulk defects					
(1) Type	**Double (D)**	**Double (D)**	**Single (A)**	**Single (A)**	**Single (A)**
	In$_{Cu}$	**In$_{Cu}$**			
σ_e (cm^2)	1.0×10^{-13}	1.0×10^{-13}	1.0×10^{-15} [12]	1.0×10^{-15} [12]	1.0×10^{-15} [12]
σ_h (cm^2)	1.0×10^{-15}	1.0×10^{-15}	5.0×10^{-13} [12]	5.0×10^{-13} [12]	5.0×10^{-13} [12]
E_t (eV)	E_c−0.25/E_c −0.34	E_c −0.25/E_c −0.34	mid-gap [12]	mid-gap [12]	mid-gap [12]
N_t (cm^{-3})	1.0×10^{13}	1.0×10^{13}	3.0×10^{17}	1.0×10^{16} [12]	1.0×10^{16} [12]
(2) Type	**Double (A)**	**Double (A)**			
	Cu$_{In}$	**Cu$_{In}$**			
σ_e (cm^2)	1.0×10^{-15}	1.0×10^{-15}			
σ_h (cm^2)	1.0×10^{-13}	1.0×10^{-13}			
E_t (eV)	E_v +0.29/E_v +0.58	E_v +0.29/E_v +0.58			
N_t (cm^{-3})	1.0×10^{13}	1.0×10^{13}			
(3) Type	**Single (A/D)**	**Single(A/D)**			
	GB	**GB**			
σ_e (cm^2)	1.0×10^{-15}	1.0×10^{-15}			
σ_h (cm^2)	1.0×10^{-15}	1.0×10^{-15}			
E_t (eV)	E_v + 0.27	E_v + 0.27			
N_t (cm^{-3})	1.0×10^{14}–1.0×10^{13} (Mo → SDL)	1.0×10^{13}			
Contacts					
		Rear			**Front**
e-*SRV* (cm·s^{-1})		1.0×10^7			1.0×10^7
h-*SRV* (cm·s^{-1})		1.0×10^7			1.0×10^7
Reflection (%)		FDTD			FDTD

having a high concentration of Ga at the rear of the CIGS such preferential movement of the electrons follow the direction away from the recombinative rear interface [57]. Additionally, the advantages of the said bandgap tuning into the absorber layer depth over a linear Ga-profile alternative, include: i) improved current density due to the increased optical absorption in the notch since this region as a low bandgap value,; ii) and high open-circuit voltage (V_{oc}) due to the higher bandgap value in the space charge region (SCR) [57]. It is important to include such feature into the electrical model, which is implemented according to the GGI profile from the ZSW experimental high-efficiency solar cell devices [7,8,25] and other literature studies [18,47,57]. The respective bandgap energy values are present in Table 1, with the notch position placed at 0.25 μm from the p-n heterojunction. While it is known that other gradients, in particular more abrupt ones, would allow for devices with better performance [57], there are experimental limitations that prevent the use of these theoretical gradients. The defined minimum bandgap value allowed the model to describe the external quantum efficiency (EQE) from the ZSW 22.6% efficient cell at the wavelength cut-off region [58].

The CdS doping and compensating defect density follow simulation studies that implement a high density of compensating defects [7,22,59, 60], which allow for a smoother band bending at the CdS layer, and the dielectric permittivity was defined according to other literature [53,61].

Several studies report the existence of a spike in the CBM level at the p-n heterojunction, i.e. the conduction band offset (CBO) at the CIGS (/SDL)/CdS interface [4,5,62,63], related to experimental solar cells with high power conversion efficiency values. With SCAPS, the spike is implemented by the difference between the respective electron affinities (χ_a), $\chi_{a\,CIGS(/SDL)} - \chi_{a\,CdS}$. Additionally, an exhaustive simulation study [4] predicts a CBO at the buffer/window interface higher or equal than − 0.1 eV also in high-efficiency devices. Therefore, the CBO values at the CIGS(/SDL)/CdS and CdS/ZMO interfaces were set to $\chi_{a\,CIGS(/SDL)} - \chi_{a\,CdS} = 0.2$ and $\chi_{a\,CdS} - \chi_{a\,ZMO} = -0.1$ eV, as respectively shown in Fig. 2. The two different referred properties, i.e. the spike at the CIGS (/SDL)/CdS interface and the CdS/ZMO CBO value, may result in the same outcome, namely the reduction of the p-n junction interface recombination [4,12].

The figures of merit values of the starting point model with referred implementations are shown in Table 2, with a power conversion efficiency (η) value of 18.8%, which is already a higher value than the one obtained by Pettersson's (17%). Note that all the simulations were performed under normal operating conditions, i.e. at room temperature and with AM1.5G solar spectrum.
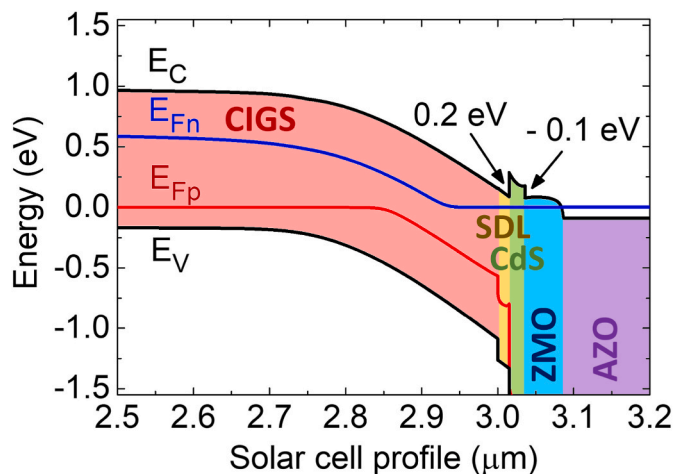
Fig. 2. Band diagram implemented in the model present in this study. E_{Fn} and E_{Fp} are quasi-Fermi levels for electrons and holes, respectively, E_C is the energy level at the conduction band minimum, and E_V is the energy level at the valence band maximum. The color for each layer is the same as in Fig. 1: red for CIGS; yellow for SDL; green for CdS; blue for ZMO; and purple for AZO. The value of 0 μm of the x axis outside the figure is placed at the Mo/CIGS interface. (For interpretation of the references to color in this figure legend, the reader is referred to the Web version of this article.)

Table 2
Model simulations results with the various consecutive updates to achieve the final baseline model. In the starting point, the CIGS defects used are the same as in Ref. [12].

Update	Model	V_{oc} (mV)	J_{sc} (mA·cm^{-2})	FF (%)	η (%)
Starting point	Single bulk defect	646	36.8	78.9	18.8
1	Double defects + GB defects	622	36.8	79.2	18.1
2(i)	Shallow defects grading with n-type inversion	641	36.6	80.9	19.0
2(ii)	Shallow defects grading without n-type inversion	645	36.6	80.5	19.0
3(i)	GB passivation	733	38.1	81.7	22.8
3(ii)	GB passivation grading	740	38.1	81.3	22.9
4	Ef pinning removal	739	38.1	81.3	22.9

2.2. Deep bulk defects

From the model attained in the Starting Point sub-section, primary model parameters to describe thin-film high-efficiency devices will be optimized and successively added and/or changed (updates), and the respective impact on the model performance will be addressed.

Previous baseline models only consider one CIGS bulk defect to account for carriers recombination [12,22]. However, this study follows a different approach to CIGS deep bulk defects as they are addressed by reported defects [13,17,64–67] both with theoretical and experimental evidence. The CIGS-based CuInSe$_2$ chalcopyrite semiconductor has several native point defects and the energy level values of many of such defects were calculated by Zhang et al. [13] and compared with experimental findings. Furthermore, the low formation energy of the V_{Cu}, In$_{Cu}$, and Cu$_{In}$ defects makes them very likely to occur in CIGS [13]. The double donor In$_{Cu}$ and double acceptor Cu$_{In}$ antisite defects have two transition energy levels, below the conduction band minimum (E_c) and above the valence band maximum (E_v) energy levels, respectively [13,66,68]. The density of such double defects are experimentally reported elsewhere [13,64,65]. The experimental values for electron/hole cross-section ($\sigma_{e/h}$) for the same CIGS defects are scarce. Therefore, the $\sigma_{e/h}$ kept the previous values in Ref. [12], presented in Table 1, and takes

into account the attractive capture cross-sections equation in Ref. [22] which relates charge carriers with defects. The very shallow acceptor V_{Cu} defect (placed at $E_v + 0.03$ eV) is addressed in SCAPS with a dedicated feature to shallow defects and has effect on the net free carrier concentration. To prevent the model from becoming too complex, only single or double defects are considered.

At this point, the model describes the influence of bulk defects: shallow V_{Cu} and double donors and acceptors, In$_{Cu}$ and Cu$_{In}$, respectively. Notwithstanding, the reported defects model by Zhang et al. [13] considers a single crystal framework. Thus, in order to describe the polycrystalline CIGS nature typically used in functional solar cells, the grain boundary (GB) effect must be considered in the final model [69, 70]. The GB effect degrading the cell performance is the band bending with barrier heights around 100 meV at the interface of two grain regions [71–73]. Hence, the SCAPS model implements the GB defect as reported elsewhere [3,69] to account for the GB band bending and by distributing the density equally between acceptors and donors [69]. The electrical model includes the GB defects as a CIGS bulk defect, considering columnar grains with 2 μm width value [69]. Such conversion from interface into bulk defects may be achieved by calculating the ratio of the respective defect density at the GB interface (2×10^{12} cm^{-2}) to the columnar grain width [69], which allows to obtain a GB defect density at the CIGS bulk. Note that this path provides the effect of GB defects in such 1D simulation. Hence, the proposed model distinguishes the CIGS defects that are, and are not, directly related with the polycrystalline nature of this absorber, GB and native defects, respectively.

Table 2 shows that, by comparing the simulated figures of merit values with the model as described in the Starting Point sub-section, and the update 1 where the impact of double donor/acceptor and GB defects is added, the V_{oc} value is significantly lower in the latter case comparing to the starting point. The lower V_{oc} obtained with the experimental-based double native and GB defects suggests that in these devices the V_{oc} value is limited by bulk recombination, and previous models underestimate the impact of CIGS native point defects and GB's in the active recombination mechanisms. Note that in Table 2 at update 1, the efficiency numbers are typical of non-anti reflection and non-PDT devices [23,74,75] considering that the common anti-reflective (AR) layer normally increases the absolute cell efficiency by 1.0–1.2% [76].

2.3. PDT effects

PDT effects on CIGS solar cells within the SCAPS model are addressed next, namely: i) a possible n-type inversion at the surface of the CIGS (/SDL) layer; ii) the increased net free carrier concentration in PDT treated devices; iii) and, the passivating effects both at the CIGS bulk and near the p-n junction interface. The PDT is linked to the recent improvement in the η value in CIGS technology. However, an adequate study of the PDT effect implies an update in the shallow acceptor defects considerations, defined in the model by the V_{Cu}.

V_{Cu} shallow acceptor defects have a great effect on the net free carrier concentration and define the p-type behavior of CIGS solar cells [13]. Furthermore, previous baseline models typically define a constant density value for the shallow acceptors through the CIGS layer [12,22]. This study addresses the latter parameter with a different approach. According to reported capacitance-voltage (C–V) measurements in complete solar cells, the CIGS net free carrier concentration varies in the CIGS depth considering the distance from the pn-junction [9,77]. So, the updated shallow acceptors density profile in CIGS depth is shown in Fig. 3 a), to describe the free carrier concentration experimentally obtained. Moreover, donor defects with shallow transition energy levels, which compensate the shallow acceptors already present in the model, were incorporated into the updated model. The respective defects density is present in Fig. 3 a) and has the same order of magnitude than the shallow acceptors one [7]. The compensating defects may be originated from Se vacancies (V$_{Se}$) shallow donor defects [13,17].

The PDT process was shown to increase the hole net free carrier
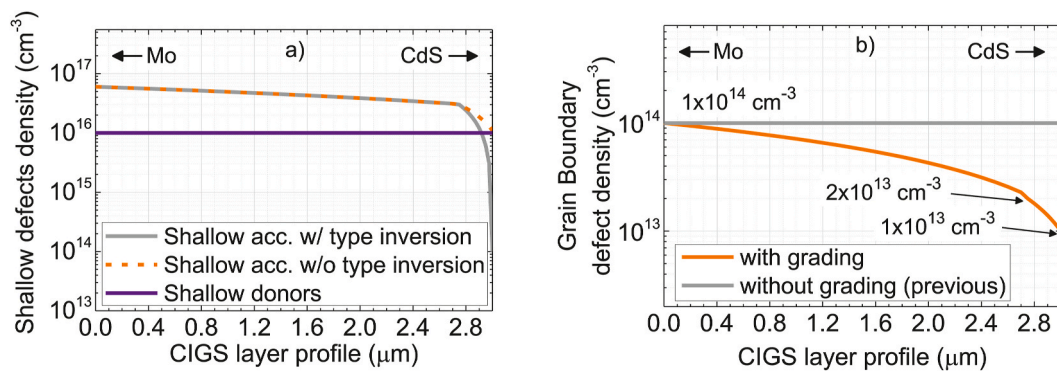
Fig. 3. a) Shallow acceptors and donors defect density profile throughout the CIGS layer from update 2. The cases with and without n-type inversion are compared. b) GB defect passivation density from update 3(i) compared with the implemented GB passivation grading at update 3(ii). Note that the GB defect density is divided in two halves, acceptor and donor defects.

concentration [7,9,78] in the CIGS bulk. Moreover, the PDT further induces the Cu-depletion at the CIGS surface which allows the diffusion of Cd during the CdS deposition, occupying the V_{Cu} and forming Cd_{Cu} antisite shallow donor defects [9,20,21,50]. But the question if the quantity of Cd atoms diffusing into the CIGS is sufficient to cause a n-type inversion at the CIGS surface is highly debatable [79], therefore the two situations: (i) with and (ii) without n-type inversion at the CIGS (/SDL) surface are compared, see Fig. 3 a), and the results presented in Table 2 as update 2 (i) and (ii), respectively. Note that a high net free carrier concentration compared to the former baseline model [12] is already incorporated in the results with the n-type inversion analysis in Table 2.

The shallow defects model update, specifically the net free carrier concentration increase, led to increased V_{oc} and fill factor (FF) values, update 1 versus update 2(i) and 2(ii) in Table 2. The high net free carrier concentration pushes the holes' quasi-Fermi energy closer to E_v, which in turn, increases the splitting of the quasi-Fermi energies for holes and electrons, and thus, leads to higher V_{oc} values in the solar cell. Hence, the CIGS net free carrier concentration could be limiting the solar cell performance. Although the increased net free carrier concentration would reduce the SCR, it is not observed any impact in the J_{sc} value. The minority charge carriers' collection length is combination of the SCR length with carriers diffusion length, therefore the unaffected J_{sc} value may be explained with the higher impact of the carriers diffusion (length >1 μm) than the impact of the SCR (with <0.3 μm) in the final collection length, which may keep the cell mostly insensitive to changes in the SCR dimensions. Another outcome is the similar results between the situations (i) and (ii), with and without the n-type inversion. Note that, the thickness of n-type inverted CIGS(/SDL) surface in update 2(i) is much higher than the CdS thickness, to demonstrate that even with such thick n-type CIGS(/SDL) surface, the impact of the n-type inversion is rather low. So, for the next steps, the shallow acceptors without the n-type inversion profile will be considered in the final model.

PDT, with heavy alkali compounds may induce the formation of secondary phases with heavy alkalies, which passivate and protect the solar cell from the already referred harmful GB defects as experimentally reported [80,81]. Such PDT effect may decrease the charge defects density at the GB and the respective band bending. In sub-section 2.2, the GB effect on the SCAPS model was already implemented, therefore the referred GB passivation is obtained by decreasing the respective GB defect density, in update 3. Moreover, Taretto et al. analysed GB defect density values inside the variation range of this study [69]. The update 2 (ii) and 3(i) results in Table 2, i.e., the model results without and with the GB passivation, respectively, show that despite the improved J_{sc} and FF values, the V_{oc} gain stands out. The great V_{oc} increase due to PDT is also reported in other literature contributions [9,78,80,81], where such strong effect of GB passivation stems from the reduced recombination at the CIGS bulk, which were limiting the cell performance. Moreover, the

GB passivation improves the η value by 3.8%, in agreement with the relation between the champion cells without and with PDT, ~20% [23] versus ~23% [2], respectively. The enhancement in the J_{sc} value is related to the increase of the minority carriers' diffusion length due to a lower recombination rate in the bulk region, and thus, an increased collection probability. Such assumption is supported by the overall increase of the external quantum efficiency (EQE) for wavelength values higher than 600 nm with GB passivation implemented.

Perceiving the PDT impact mainly on the CIGS surface, Tai et al. from Solar Frontier reported a reduced interface and SCR recombination with this treatment [59], where the simulated density of the deep CIGS defects decreases from the Mo contact to CdS. To update the model with an equivalent effect, we considered that PDT has a major impact in passivating the GBs [80,81] therefore, as the grading profile in Fig. 3 b) shows, the defect density is linearly reduced toward the p-n junction. The defect density values are also present in Table 1. The update 3(ii) in Table 2 corresponds to the model results with the incorporation of the GB defect density grading, where opposite effects are observed by comparing with the V_{oc} and FF values in update 3(i). Moreover, the unaltered J_{sc} value, together with the impact on both V_{oc} and FF, resulted in 0.1% increase of power conversion efficiency, which may stem from the reduction of recombination around the SCR. Nevertheless, the update 3(ii) result has closer V_{oc} and FF values with the thin-film champion cell from ZSW (22.6%) [25]. The conversion efficiency improvement obtained with the PDT bulk effects is much higher, than the one obtained with PDT interface effects. Note that the impact of n-type inversion at the CIGS surface was regarded as PDT interface effect, whereas the increased net free carrier concentration was considered as a PDT bulk effect. Hence, the model predicts higher impact on cell performance from PDT bulk effects compared to the interface effects, which agrees well with a recent study [80].

It is important to mention that until now the model of this study, as in Pettersson's model, contains an interface donor-like defect at the p-n heterojunction to implement the effect of the Fermi energy (E_F) pinning. The E_F pinning at the CIGS(/SDL)/CdS interface consists of a specific position or a discrete number of possible positions at this interface where the E_F is fixed, due to the respective interface defects level, exemplified in the literature [82]. The referred interface defect is placed near E_c and has low σ_e and σ_h values to pin E_F. However, the E_F pinning is a much-debated property [12,60]. Furthermore, through Table 2 the effect of E_F pinning is negligible on the devices' figures of merit and shows no influence on the solar cell band diagram. Therefore, in this study, the donor-like interface defect was not considered. The model performance after the update of the CIGS defects and the PDT effects already shows similar results compared with the champion cell [25], which indicates a good CIGS solar cell modelling. However, the optical rear and front reflection data lacks optimization as both parameters are set to 0%.

2.4. FDTD 3D optical simulations support

The rear and front optical reflection values used for the baseline model are obtained through FDTD simulation results. We note that in SCAPS, a bandgap grading profile in CIGS was defined according to the experimental high-efficiency solar cells referred in section 2.1. However, in the FDTD simulations, it was only considered the bandgap value at the CIGS surface in contact with the CdS layer, as the CIGS optical constants at this surface influence the front reflection. The replication of a grading bandgap profile in the *Lumerical* FDTD software produced additional unrealistic interference fringes in the optical reflection data at the IR wavelength range values and more complexity to simulation process.

A background medium with a suitable refractive index (n) considering the CIGS GGI composition was used to simulate the Mo/MoSe$_2$ reflection through the *Lumerical* FDTD software. The value of n corresponds to the average value of the CIGS material near the rear contact for the studied GGI ratio. The fixed n is an approximation as this index varies with wavelength (n variation of 2.8–3.2). A MoSe$_2$ layer of 2 nm was added to the optical simulations due to the experimental selenization of the Mo rear contact that occurs during the CIGS growth [83]. The rear optical reflection is presented in Fig. 4 a), together with the impact in the EQE curve, which may be seen by comparing both EQE curves inside the figure, one for the model with the implemented rear optical reflection and the other with the same reflection set at 0%. The higher EQE value with the FDTD simulated reflection for wavelength values higher than 950 nm, is compatible with an improvement in the IR light absorption. The simulated rear reflection describes with more accuracy a real device behavior, i.e. the IR light radiation has higher probability of reaching the Mo rear contact, enabling a second pass for the fraction of reflected light into the CIGS absorber, increasing its probability to be absorbed.

Regarding the front reflection, to obtain an experimentally based model that can be compared with high-efficiency CIGS solar cells, an AR layer of MgF$_2$ was implemented at the front contact. Furthermore, the

thickness of the assumed layer was optimized to achieve the highest J_{sc} value. The optimization of the AR layer is demonstrated in Fig. 4 b), where the EQE curves for different AR layer thicknesses are presented together with the respective J_{sc} values. Fig. 4 b) shows the effect of the interference fringes on EQE caused by the upper layers of the solar cell. Higher AR layer thickness values provide a better fit at long wavelength values with the champion cell EQE curve (not shown here), whereas at shorter wavelength values a good fit is possible for lower thickness values. Nonetheless, the optimized layer that provides the highest J_{sc} value is represented in the same Fig. 4 b), with 115 nm of thickness. A step further, the CIGS roughness from a complete solar cell is provided by atomic force microscopy from in-house experimental measurements, which was then implemented in the FDTD optical simulations. The front optical reflection with the aforementioned optimizations is presented in Fig. 4 c). The impact of the front reflection update on the EQE is observed by comparing the curve with the fully optimized rear and front reflections with the one where just the rear reflection is optimized. A good fit is achieved between the final EQE response curve obtained from the SCAPS model and from the ZSW 22.6% efficient cell presented in Ref. [58]. However, the interference fringes are still not similar between both curves, which is explained by different CIGS roughness that is rather variable and process dependent. The results in Table 3 show that by incorporating FDTD simulation results in the SCAPS model, it is possible to obtain an electrical model that describes the behavior of experimental high-efficiency solar cell devices. Hence, the V_{oc} and *FF*

Table 3
Comparison of the final SCAPS baseline model performance with the champion solar cell with the same architecture [25]. The values in brackets are the J_{sc} and η value with 1.7% grid coverage characteristic of real devices [84].

Model	V_{oc} (mV)	J_{sc} (mA·cm^{-2})	*FF* (%)	η (%)
SCAPS baseline model	738	37.0 (36.4)	81.4	22.3 (21.9)
Champion solar cell	741	37.8	80.6	22.6
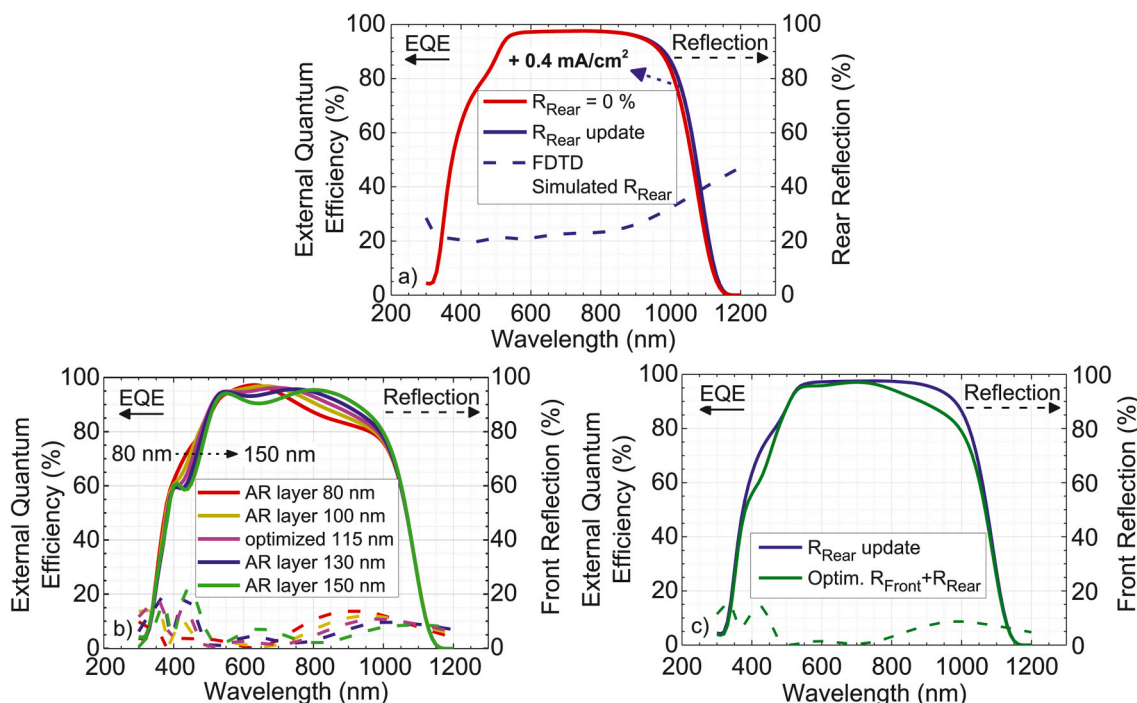
Fig. 4. EQE response curves for different optimization stages of the rear (R$_{Rear}$) and front (R$_{Front}$) optical reflection and respective values implemented into the SCAPS model: a) rear reflection updated from FDTD simulation results, note that, so far, the front reflection is set to 0%; b) optimization of the AR layer to achieve the best J_{sc} value, where the respective thickness is varied with 80 nm (J_{sc} value of 36.06 mA cm^{-2}), 100 nm (36.51 mA cm^{-2}), the optimized 115 nm (36.61 mA cm^{-2}), 130 nm (36.55 mA cm^{-2}), and 150 nm (36.31 mA cm^{-2}); and c) final front reflection optimization with the introduction of CIGS roughness in the FDTD simulation and comparison with the previous step a). The introduction of the CIGS roughness improved the J_{sc} value by 0.4 mA cm^{-2}.

Fig. 5. Updating steps necessary to perform in the SCAPS model from the previous Pettersson's model to the validation with the champion thin-film solar cell.

values are well modelled, mainly due to the updated parameters, namely from CIGS deep bulk defects, PDT bulk and surface effects, and also from FDTD 3D optical simulations support. The J_{sc} value was corrected to account for the grid shadow and is shown in parenthesis in Table 3. SCAPS does not consider any shadow generated by the front grid contacts in real devices, therefore 1.7% of the current density value is reduced due to the same value grid coverage [84]. The J_{sc} value is slightly lower than the experimental one. A possible explanation may stem from the optical constants considered for the CIGS layer [51], which yields lower values compared to another study [53], however, the optical data from Fujiwara et al. for CIGS is rather complete with many optical values throughout the wavelength range of interest and for different compositional ratios of GGI and [Cu]/([Ga]+[In]) (CGI). Moreover, different CIGS roughness may also increase the current density value. Nonetheless, this study provides a pathway to a solid baseline model, which may be widely used by the community. All in all, bringing

together the electrical and optical simulation tools, SCAPS and FDTD, respectively, allows for the development of a robust model that can describe an experimental champion solar cell with the same architecture. The overall integrated updates in the baseline are summarized in Fig. 5.

3. Baseline model for ultrathin devices

The modelling process and validation with experimental results are presented here for the ultrathin best performing CIGS solar cell with 0.49 μm, which was developed at NREL with η = 15.2% [85].

Table 4 shows the steps from A to E taken to achieve the ultrathin SCAPS baseline model. From the previous model validated for high-efficiency thin-film solar cells, the CIGS thickness was reduced from 3.0 to 0.49 μm, as experimentally reported [85], where the modelled performance are presented in step A. Furthermore, the bandgap value was adapted and follows the reported GGI profile for the NREL devices, in step B. Additionally, the minimum bandgap value, i.e. the bandgap value at the notch position, was adjusted by matching the simulated EQE curve at the wavelength cut-off region with the reported EQE curve in Ref. [85], through an offset of the GGI values, and thus, the bandgap values. At step C in Table 4, the remaining layers thickness, namely CdS, i-ZnO, and AZO, were defined according with the champion ultrathin cells [75,85,86]. Note that the ZMO window layer in the thin-film model was replaced by i-ZnO, where the optical properties were obtained from Carron et al. [53]. The CdS thickness value was also optimized through its parasitic light absorption at the wavelength values between approximately 400 to 500 nm, characteristic in CIGS devices EQE curves. Considering the absence of a PDT treatment in the champion ultrathin cells, those features were removed in step D in Table 4. The exclusion of the PDT effect implied: i) a decrease on the net free carrier concentration by half to the ones defined in the thin-film model present in Table 1 [9,78]; and ii) an increase of the GB defects density to a constant value considered in section 2 for devices without PDT. Finally, at step E, taking into account the near stoichiometric CIGS composition in such NREL solar cells [85], the GB defects density was slightly reduced compared with the respective density present in the thin-film model before the PDT incorporation. Such stoichiometric CIGS compositions have CGI values near 1, which lead to Cu-richer solar cells compared with CGI values of 0.9 for the champion thin-film cell [25], and thus, larger CIGS grain sizes due to a Cu_xSe liquid-phase-assisted

Table 4
SCAPS model simulation results with the various consecutive steps to achieve the final model for ultrathin high-efficiency solar cells, validated against the NREL ultrathin champion cell [85], and the NREL ultrathin champion cell Figures of Merit.

Steps	Model	V_{oc} (mV)	J_{sc} (mA·cm^{-2})	FF (%)	η (%)
A	Ultrathin CIGS (0.49 μm)	771	28.5	81.7	18.0
B	Bandgap	798	26.5	83.2	17.6
C	Window/buffer layers thickness	802	25.3	83.6	17.0
D	PDT removal	722	25.3	80.9	14.9
E	GB defect density decrease	734	25.3	80.9	15.1
–	NREL champion cell [85]	733 ± 1	26.4 ± 0.2	78.2 ± 0.3	15.2 ± 0.1

Table 5
Adapted parameters in the SCAPS model for the ultrathin champion cell in Ref. [85] from the thin-film model (TF) in Table 1.

Layer properties	CIGS	SDL	CdS	i-ZnO	AZO
Thickness (μm)	0.49	0.015	0.05	0.05	0.35
E_g (eV)	Graded [85]	TF	TF	TF	TF
χ_a (eV)	Graded	4.31	4.11	4.21	4.21
N_D (cm^{-3})	5.00×10^{15}	5.00×10^{15}	TF	TF	TF
N_A (cm^{-3})	3.00×10^{16}–5.50×10^{15} (Mo → SDL)	5.50×10^{15}	–	–	–
Bulk defects					
(3) Type	**Single (A/D)**	**Single(A/D)**			
	GB	**GB**			
N_t (cm^{-3})	7.00×10^{15}	7.00×10^{15}			

CIGS film growth [87,88]. Ultimately, the larger CIGS grain sizes will lead to a lower density of GB throughout the CIGS absorber material. Table 5 summarizes all the model parameters that were adapted in order to describe the champion ultrathin CIGS solar cells. Once again, the MgF_2 AR layer thickness value was optimized for the architecture of the champion ultrathin solar cell.

The step A in Table 4 reveals that with the absorber thickness reduction alone, the figures of merit values do not describe real ultrathin devices with about 0.5 μm of thickness in the absorber layer until the moment of writing of this study. Therefore, it is important to take a deep look into the ultrathin model, and in this case, a deep look into the champion ultrathin solar cell. The result of the bandgap value optimization according to the experimental solar cell in step B led to the increase of V_{oc} and the decrease of J_{sc} values. The referred figures of merit variation stems from the overall higher bandgap value that was obtained in the optimization of the fabrication process introduced in the champion ultrathin cell and named as the CoEvap deposition method in [85], compared to the thin-film model. Mansfield et al. [85] developed a CIGS absorber device with a linear GGI profile with overall higher Ga composition values, which was implemented in the SCAPS model. At step C, the J_{sc} value also decreased due to the increased CdS and AZO layers thickness values compared with the champion thin-film cell. Finally, with the PDT impact excluded at step D, we achieve closer values in V_{oc} and FF. Moreover, when the SCAPS model considered the near stoichiometric CIGS composition of the champion NREL solar cell, the figures of merit values were further optimized, except the J_{sc} value. The losses in J_{sc} mainly occur in the wavelength region between 600 and 1000 nm according to the experimental and simulated EQE curves, which are related to the poor CIGS light absorption. Therefore, the explanation for the lower J_{sc} value in the electrical model may stem from i) a possible deviation in the CIGS thickness measurement toward increased values than 0.49 μm, ii) an increased rear reflection in the experimental soda-lime glass/Mo substrate, and iii) related with the optical constants considered for the CIGS layer [51]. It is important to note that if this ultrathin model incorporated R_s and R_{sh} values characteristic of high-performing solar cells [89], the FF value would move toward the experimental one.

Despite the difference in the J_{sc} value, the core parameters of the electrical SCAPS model are validated also for ultrathin high-efficiency CIGS solar cells. Such an electrical model built through several slices allows to describe and adapt to the experimental optimizations, which in turn makes it able to keep up with the technology development. The champion ultrathin cell does not have a PDT treatment nor the incorporation of passivation or light management strategies, which indicate further potential for improvement and even achieve similar performance compared with the thicker counterparts [2,25]. Finally, this ultrathin model may pave the way for a baseline model with ultrathin CIGS absorbers.

4. Limitations of ultrathin solar cells

Limiting performance factors in ultrathin CIGS solar cells will be highlighted and discussed through the point of view of SCAPS simulations. Therefore, the effect on cell performance of optical and electrical properties will be assessed, aiming to achieve a high-efficiency ultrathin device and a better understanding on the impact of the respective strategies.

4.1. Optical limitations

Several factors contribute to the optical losses in ultrathin solar cells. The ultrathin CIGS is unable to fully absorb the incoming photons for wavelength values higher than 600 nm, which, by coupling with the poor optical reflection of Mo, increases the parasitic absorption by the rear contact. Moreover, unlike thicker solar cells, a higher fraction of minority carriers is generated near the rear contact, which increases the carriers' recombination at this rear interface [29]. Fortunately, the said optical losses can be mitigated with the application of light management
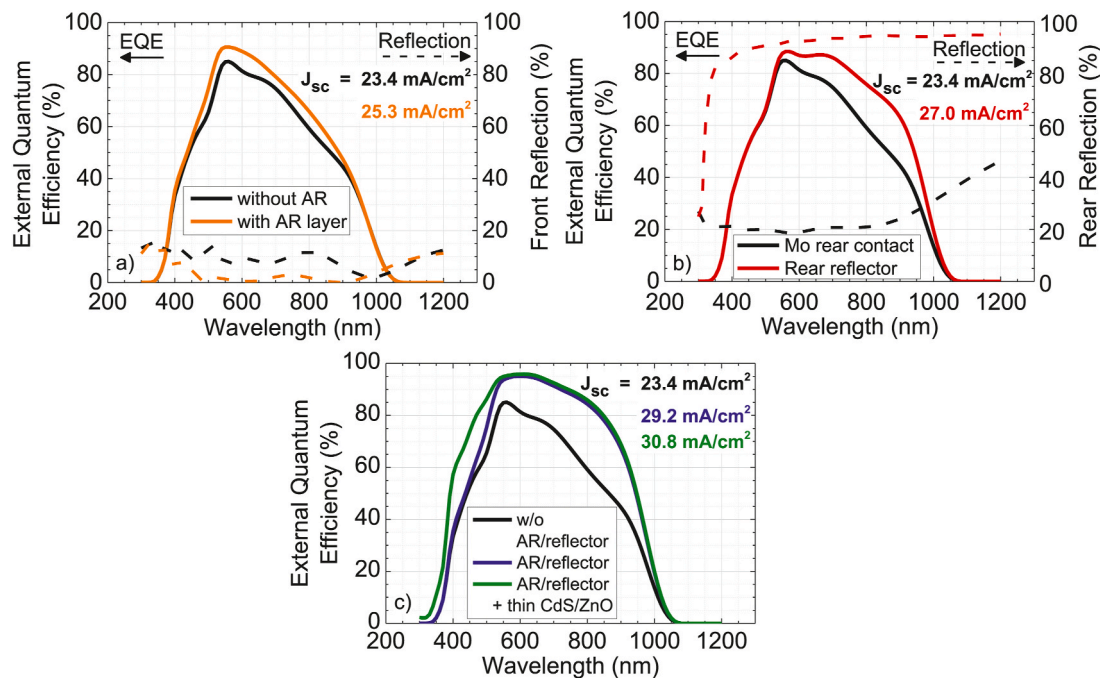

Fig. 6. EQE curves for the study of the AR layer at the front contact (a), optical optimization at the rear contact (b)) through the implementation of silver/dielectric structure and without the AR layer, and (c)) the full optical optimization at both contacts. The optical reflections obtained with FDTD and incorporated into SCAPS are also presented together with the respective EQE curves. J_{sc} values are present inset. Finally, in c) to obtain the green curve EQE result, the model implemented thinner CdS and ZnO layers, with the same thickness as in Table 1. The simulation results presented in this figure use solar cell models with 0.49 μm of CIGS thickness, as in the ultrathin SCAPS baseline model above. (For interpretation of the references to color in this figure legend, the reader is referred to the Web version of this article.)

techniques at rear and front contacts [29,30,32,36].

Fig. 6 shows the EQE curves, contacts' reflection, and respective J_{sc} values, which address the impact of the AR layer in Fig. 6 a), the impact of the rear reflector incorporation in Fig. 6 b), and the combined effect of both strategies in Fig. 6 c). The SCAPS ultrathin model is tested both with and without the AR layer to address the impact of such layer. Note that the ultrathin model in the previous section implemented this AR layer, and thus, already benefits from the lower front reflection. The simulated EQE curves in Fig. 6 a) show that the presence of an AR layer increases the J_{sc} value by 1.9 mA/cm^2, from 23.4 mA cm^{-2} to 25.3 mA cm^{-2}, respectively. Finally, additional steps to improve the cell anti-reflection properties may include a nanostructured TCO window layer with 2D triangular gratings and an optimized period [31], with the advantage of reducing front reflection losses for a wide range of incident light angles.

On the other hand, to enhance the J_{sc} value in ultrathin devices, one may introduce a highly reflective layer at the rear contact, i.e. a rear reflector. In such ultrathin cells, the rear reflector magnifies the J_{sc} value benefit effect more than in thicker cells, as in the former the already referred longer wavelength photons have lower probability of being absorbed in the first passage through the ultrathin absorber [36,90]. To model such a rear reflector, FDTD optical simulations were used. The rear reflection for a rear double structure was made of a silver metal with a thickness of 50 nm, deposited between the Mo rear contact and 20 nm of a dielectric passivating layer. Fig. 6 a) shows that the presence of the rear contact reflector increases the J_{sc} value by 3.6 mA/cm^2, from 23.4 mA cm^{-2} to 27.0 mA cm^{-2}, without considering an AR layer. Note that due to the CIGS harsh growth conditions, the silver deposited at the rear contact must have a diffusion blocking layer to prevent reaction with CIGS, which may be obtained with an encapsulating dielectric layer [30, 36]. Moreover, the referred dielectric layer may passivate the rear interface defects, which in turn improves the J_{sc} value by the increase in the minority carriers' collection [33]. The contact nanopattern follows the passivation structure dimensions fabricated by Lopes et al. [27]. In SCAPS, the passivation effect is implemented by varying the surface recombination velocity (SRV) at the rear contact for the minority carriers. Therefore, the simulation with the double metal/dielectric structure has a SRV value of 10^2 cm s^{-1} in opposition to the non-passivated devices with a value of 10^7 cm s^{-1}.

The incorporation of the optical optimizations referred in this sub-section, at the rear and front contacts, in ultrathin devices may tackle the inherent light absorption losses. Therefore, high rear reflection values together with low front reflection values may increase the J_{sc} value from 23.4 to 29.2 mA cm^{-2}, corresponding to 13.9% and 17.6% efficiency, respectively, as demonstrated above. Finally, further optimization may be attained by reducing the parasitic absorption of the CdS and ZnO layer through the reduction of their thickness to the values shown in Table 1, resulting in the J_{sc} value of 30.8 mA cm^{-2} (18.6% efficiency). Itshould be noted that a simplistic simulated approach to increase optical properties due to the 1D simulation nature was used, thus additional more complex strategies such as the incorporation of nanoparticles [31] would also improve the J_{sc} value.

The ultrathin cell J_{sc} value is about 30% lower than the champion thin-film cell. This loss is partially recovered after the implementation of the rear reflector and thinner buffer and window layers (15% loss). Although the J_{sc} performance may be further improved with additional light management strategies, it comes at the expense of additional fabrication complexity and costs. As such, it is relevant to evaluate if these light management strategies could be mitigated by using a thicker absorber. Thus, we study the J_{sc} and V_{oc} for intermediate absorber thickness values to speculate on the fabrication costs and industrial application. Without effective light management in the ultrathin cells, there will be a compromise between the high V_{oc} values of the ultrathin devices and the high J_{sc} values of the thin-film ones. Fig. 7 shows the solar cell performance for different CIGS thickness values from ultrathin to thicker absorbers with an optimized architecture (rear reflector,
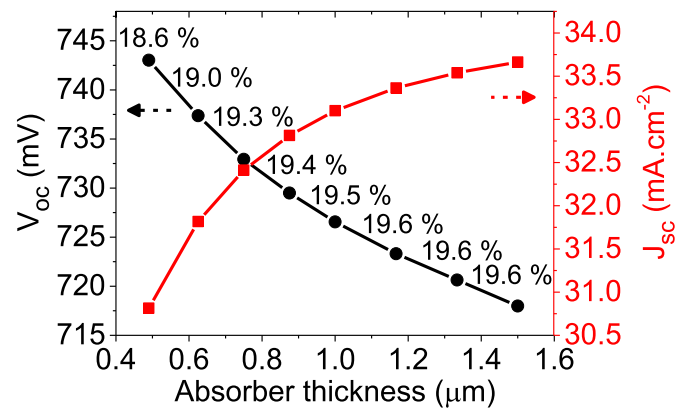

Fig. 7. V_{oc} and J_{sc} performance for different CIGS absorber thickness values according to the SCAPS model with all the optimizations referred in sub-section 4.1 for ultrathin devices. Note that the rear contact is providing for a high optical reflection. The percentage values inset correspond to respective cell conversion efficiency.

passivation, and thin buffer and window layers). It is clearly demonstrated the inverse correlation of V_{oc} with J_{sc} as the CIGS thickness varies, which stems from both effects of increased bulk recombination [91] and light absorption for thicker absorbers. Regarding the industrial and scientific perspectives, a CIGS thickness of about 1.0 μm may hold the best compromise on fabrication costs and cell performance, as the cell benefits from high V_{oc} and J_{sc} values, with a J_{sc} loss lower than 10% compared to thicker solar cells. We also note that the efficiency appears to plateau around 19.6%, a value far away from the record 23.35%, which further demonstrates that there are significant optoelectronic gains to be made in the ultrathin as its model do not reflect the best cells for thick devices.

4.2. Recombination losses limitations

The reduced distance between the heterojunction and the rear contact in ultrathin solar cells leads to an increased sensibility of these devices to the minority carriers' recombination at the rear contact, due to the higher number of photons being absorbed near the rear contact/ CIGS interface. Fig. 8 a) plots the V_{oc} and η results for varied rear SRV values to assess its impact on the ultrathin cell performance. The SRV variation includes only electrical effects of rear passivation and discards the optical ones, such as an increase in optical reflection. Fig. 8 a) shows that the performance reaches a plateau for SRV lower than 10^4 cm s^{-1}, in such regime the optical properties gain a more prominent role at enhancing the performance. It is common in rear passivated devices to have recombination velocity values lower than 10^4 cm s^{-1}, down to 10^2 cm s^{-1} [92,93]. Therefore, there is the possibility for the fabrication of passivated ultrathin solar cells, that may fully exploit the impact of a lower rear recombination probability. Nonetheless, the impact of the rear recombination on such high-efficiency ultrathin cells performance is not as high as the impact of the bulk recombination. Such result indicates that the recombination at the bulk may be limiting the performance of champion ultrathin solar cells, which would benefit of an improved CIGS absorber quality.

Fig. 8b) and c) present the J-V curves and the figures of merit values by varying the GB bulk defect density for the situations without and with rear passivation, i.e. with SRV of 10^7 and 10^2 cm s^{-1}, respectively, which means that Fig. 8b) and c) are two particular cases in terms of SRV values of Fig. 8 a). The performance of the modelled ultrathin solar cells increases by reducing the GB defect density values for both situations. However, the J-V curves in Fig. 8 c) demonstrates that the rear passivation potentiates the impact of the reduced bulk defect density, i.e. bulk recombination probability, on the cell performance. Otherwise, Fig. 8b) and c) show that a less defective CIGS layer also potentiates the rear
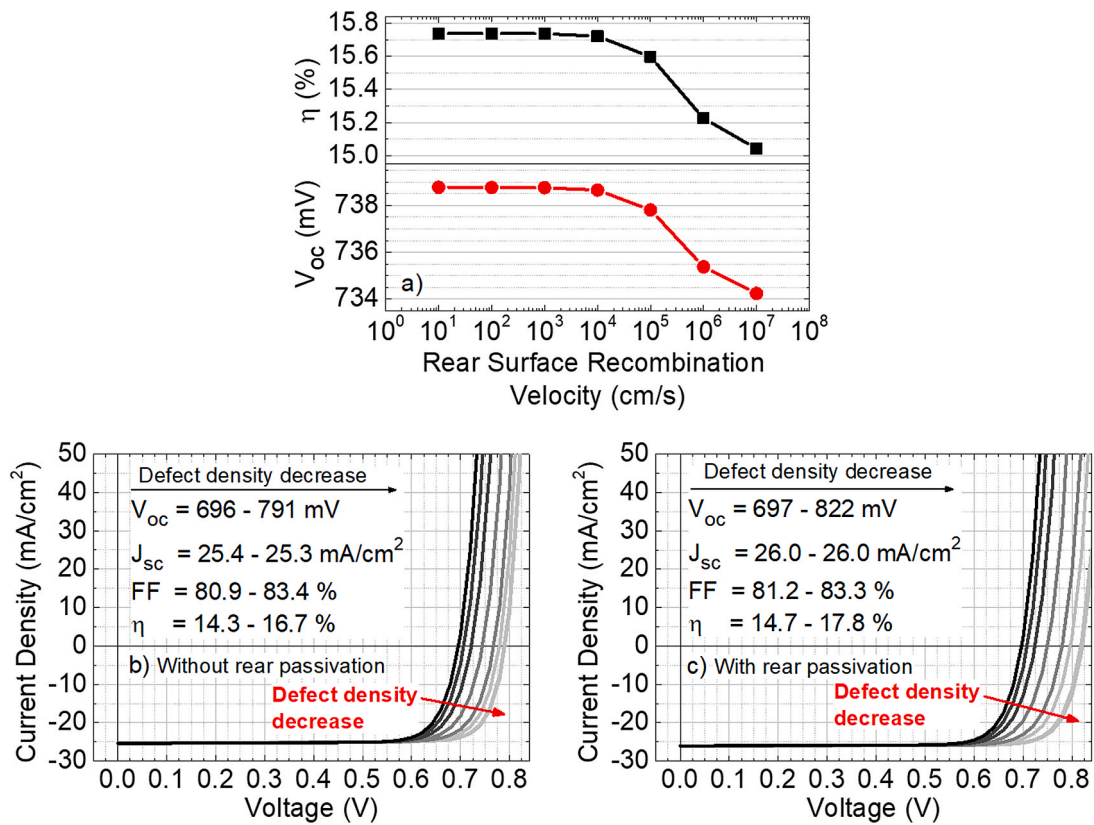
Fig. 8. a) Figures of merit values for varying rear recombination velocity values. JV curves for different GB defect density values with the figures of merit inset (b) and c)) for the ultrathin model without (b)) and with (c)) rear passivation, i.e., with *SRV* values of 10^7 and 10^2 cm s^{-1}, respectively. Note that the for the lowest defect density, the V_{oc} value is higher than the champion cell from the thicker counterpart devices.

passivation effect, as seen by the 31 mV difference on the respective highest V_{oc} values at the inset tables (791 vs 822 mV). The PDT already implemented in the thin-film SCAPS model may be suggested to improve the CIGS bulk properties if optimized for ultrathin cells, as it would passivate GB defects. Hence, this study shows the importance of the rear passivation and optimized PDT joint strategies in ultrathin CIGS solar cells, also reported elsewhere [27].

By merging all mentioned optical and electrical optimizations, ultrathin solar cells may achieve an efficiency of 21.0% which is +5.9% abs. higher when compared with the ultrathin baseline model whose result is presented in step E of Table 4 (15.1% eff.). Note that these simulations were performed without R_s and R_{sh}, which means R_s of 0 and a sufficiently high R_{sh}, to assess the impact of the studied optical and electrical features and due to the variability of these resistance values on a specific fabrication process. The simulated V_{oc} value is above the one of the champion thin-film cell, 822 in Fig. 8 c) *versus* 741 mV respectively. This happens due to the advantage of using an ultrathin absorber, since the bulk recombination is inherently reduced [91], and even if the defect level continues high, the resulting outcome of the reduced bulk recombination may outweigh the increased defect density, resulting in a performance uplift. Therefore, if the CIGS growth quality level is kept the same between thin and ultrathin devices, the latter may even surpass the standard devices' performance, with additional benefits on lower fabrication costs, and environmental sustainability.

5. Conclusion

This study provided an update of the previous baseline electrical models with SCAPS, which was validated with the champion solar cells for both thin and ultrathin film CIGS devices. The starting point was the baseline from Pettersson et al., and from there the model was updated at the CIGS bulk defects, with the incorporation of PDT features, and with

the support from FDTD solutions software, for a robust SCAPS model, providing rear and front reflection data.

The CIGS deep bulk defects were decoupled between native point defects and GB defects, present in polycrystalline CIGS absorbers of champion cells. Therefore, we successfully incorporated the GB passivation effect of PDT which greatly improves the cell performance, together with other PDT surface effects. The PDT bulk effects had much higher impact on cell performance than PDT effects near the p-n heterojunction, with such result also supported by recent studies. With this study contribution, the community has an instrument that can be used to identify the problems and the research priority focus to overcoming them. As an example, the low impact on cell performance of PDT at the front interface identified with the SCAPS model has high relevance, as it indicates substantial potential to improve here with, e.g., a passivation layer at the p-n heterojunction [94].

The baseline for high-efficiency devices was applied and validated also to the NREL champion ultrathin solar cells. The adaptation of some parameters from the thin to the ultrathin film model was shown to be important to provide for an accurate SCAPS baseline of CIGS ultrathin devices. Therefore, such an electrical model built through several slices allows to describe and adapt to the experimental optimizations, which in turn makes it able to keep up with the technology development. Moreover, the ultrathin model paves the way for a baseline of ultrathin CIGS devices. The study of the ultrathin solar cells' limitations provided useful insight into the impact of the rear and front reflection, and the into the rear interface and bulk recombination. The SCAPS simulations suggested that the optimization on the optical reflection of both contacts, as the incorporation of a rear reflector and an optimized AR layer, may significantly improve the J_{sc} value of the ultrathin solar cell. Although is important to study two opposite CIGS thickness values of 3 and 0.49 μm, the J_{sc} value of the ultrathin cell is about 30% lower than the thicker counterpart, and thus, the best approach that do not

compromise the V_{oc} and J_{sc} performance and fabrication costs may lie in the CIGS thickness between those two extreme values. The model predicts the 1.0 μm cell to be a good choice in terms V_{oc} and J_{sc} performance, with a J_{sc} loss lower than 10% compared to the standard thicker counterparts. Simulation results on the rear *SRV* and on the CIGS bulk defects density, which may be replicated in experimental CIGS devices through rear passivation and PDT, respectively, indicate that the incorporation of both strategies is more effective in improving the device's performance compared to only one of the referred techniques. Finally, the aforementioned CIGS solar cells improvements may lead the ultrathin devices to a performance of 21.0% in conversion efficiency, which may compete with traditional devices as demonstrated by the high simulated V_{oc} value.

CRediT authorship contribution statement

André F. Violas: Writing – original draft, Methodology, Data curation, Conceptualization. **António J.N. Oliveira:** Writing – review & editing, Methodology, Data curation. **Jennifer P. Teixeira:** Writing – review & editing, Supervision, Methodology. **Tomás S. Lopes:** Writing – review & editing, Data curation. **João R.S. Barbosa:** Writing – review & editing, Data curation. **Paulo A. Fernandes:** Writing – review & editing, Supervision, Funding acquisition. **Pedro M.P. Salomé:** Writing – review & editing, Supervision, Funding acquisition, Conceptualization.

Declaration of competing interest

The authors declare that they have no known competing financial interests or personal relationships that could have appeared to influence the work reported in this paper.

Acknowledgments

References

[1] M.A. Green, E.D. Dunlop, J. Hohl-Ebinger, M. Yoshita, N. Kopidakis, X. Hao, Solar cell efficiency tables (Version 58), Prog. Photovoltaics Res. Appl. 29 (2021) 657–667, https://doi.org/10.1002/pip.3444.

[2] M. Nakamura, K. Yamaguchi, Y. Kimoto, Y. Yasaki, T. Kato, H. Sugimoto, Cd-free Cu(In,Ga)(Se,S)₂ thin-film solar cell with record efficiency of 23.35, IEEE J. Photovoltaics 9 (2019) 1863–1867, https://doi.org/10.1109/JPHOTOV.2019.2937218.

[3] G. Sozzi, F. Troni, R. Menozzi, Numerical analysis of the effect of grain size and defects on the performance of CIGS solar cells, in: Int. Conf. Compd. Semicond. Manuf. Technol. CS MANTECH, Portland, Oregon, USA, 2010.

[4] G. Sozzi, F. Troni, R. Menozzi, On the combined effects of window/buffer and buffer/absorber conduction-band offsets, buffer thickness and doping on thin-film solar cell performance, Sol. Energy Mater. Sol. Cells 121 (2014) 126–136, https://doi.org/10.1016/j.solmat.2013.10.037.

[5] G. Sozzi, S. Di Napoli, M. Enna, R. Menozzi, D. Hariskos, W. Witte, Numerical simulation of CIGS solar cells with Zn(O,S) or (Cd,Zn)S buffers and (Zn,Mg)O as high-resistive layer, in: 2019 IEEE 46th Photovolt. Spec. Conf., 2019, pp. 2155–2158, https://doi.org/10.1109/PVSC40753.2019.8980882.

[6] A. Chirilă, S. Buecheler, F. Pianezzi, P. Bloesch, C. Gretener, A.R. Uhl, C. Fella, L. Kranz, J. Perrenoud, S. Seyrling, R. Verma, S. Nishiwaki, Y.E. Romanyuk, G. Bilger, A.N. Tiwari, Highly efficient Cu(In,Ga)Se₂ solar cells grown on flexible polymer films, Nat. Mater. 10 (2011) 857–861, https://doi.org/10.1038/nmat3122.

[7] T.M. Friedlmeier, P. Jackson, A. Bauer, D. Hariskos, O. Kiowski, R. Wuerz, M. Powalla, Improved photocurrent in Cu(in,Ga)Se₂ solar cells: from 20.8% to 21.7% efficiency with CdS buffer and 21.0% Cd-free, IEEE J. Photovoltaics 5 (2015) 1487–1491, https://doi.org/10.1109/JPHOTOV.2015.2458039.

[8] T.M. Friedlmeier, P. Jackson, A. Bauer, D. Hariskos, O. Kiowski, R. Menner, R. Wuerz, M. Powalla, High-efficiency Cu(In,Ga)Se₂ solar cells, Thin Solid Films 633 (2017) 13–17, https://doi.org/10.1016/j.tsf.2016.08.021.

[9] F. Pianezzi, P. Reinhard, A. Chirilă, B. Bissig, S. Nishiwaki, S. Buecheler, A. N. Tiwari, Unveiling the effects of post-deposition treatment with different alkaline elements on the electronic properties of CIGS thin film solar cells, Phys. Chem. Chem. Phys. 16 (2014) 8843–8851, https://doi.org/10.1039/c4cp00614c.

[10] T. Kodalle, H.A. Yetkin, T. Bertram, R. Schlatmann, C.A. Kaufmann, Setting up a device model for Rb-conditioned chalcopyrite solar cells, in: 2020 47th IEEE Photovolt. Spec. Conf., 2020, pp. 1156–1162, https://doi.org/10.1109/PVSC45281.2020.9301015.

[11] M. Burgelman, P. Nollet, S. Degrave, Modelling polycrystalline semiconductor solar cells, Thin Solid Films 361–362 (2000) 527–532, https://doi.org/10.1016/S0040-6090(99)00825-1.

[12] J. Pettersson, C. Platzer-Björkman, U. Zimmermann, M. Edoff, Baseline model of graded-absorber Cu(In,Ga)Se₂ solar cells applied to cells with Zn₁ ₋ ₓMgₓO buffer layers, Thin Solid Films 519 (2011) 7476–7480, https://doi.org/10.1016/j.tsf.2010.12.141.

[13] S.B. Zhang, S.-H. Wei, A. Zunger, H. Katayama-Yoshida, Defect physics of the CuInSe₂ chalcopyrite semiconductor, Phys. Rev. B 57 (1998) 9642–9656, https://doi.org/10.1103/PhysRevB.57.9642.

[14] G. Massé, E. Redjai, Lattice defects in I-III-VI₂ compounds, J. Phys. Chem. Solid. 47 (1986) 99–104, https://doi.org/10.1016/0022-3697(86)90183-6.

[15] T. Irie, S. Endo, S. Kimura, Electrical properties of p- and n-type CuInSe₂ single crystals, Jpn. J. Appl. Phys. 18 (1979) 1303–1310, https://doi.org/10.1143/JJAP.18.1303.

[16] F. Abou-Elfotouh, D.J. Dunlavy, D. Cahen, R. Noufi, L.L. Kazmerski, K. J. Bachmann, Photoluminescence studies of CuInSe₂: identification of intrinsic defect levels, Prog. Cryst. Growth Char. 10 (1984) 365–370, https://doi.org/10.1016/0146-3535(84)90057-1.

[17] C. Rincón, R. Márquez, Defect physics of the CuInSe₂ chalcopyrite semiconductor, J. Phys. Chem. Solid. 60 (1999) 1865–1873, https://doi.org/10.1016/S0022-3697(99)00190-0.

[18] T. Dullweber, G. Hanna, U. Rau, H.W. Schock, New approach to high-efficiency solar cells by band gap grading in Cu(In,Ga)Se₂ chalcopyrite semiconductors, Sol. Energy Mater. Sol. Cells 67 (2001) 145–150, https://doi.org/10.1016/S0927-0248(00)00274-9.

[19] D. Schmid, M. Ruckh, F. Grunwald, H.W. Schock, Chalcopyrite/defect chalcopyrite heterojunctions on the basis of CuInSe₂, J. Appl. Phys. 73 (1993) 2902–2909, https://doi.org/10.1063/1.353020.

[20] J. Kiss, T. Gruhn, G. Roma, C. Felser, Theoretical study on the structure and energetics of Cd insertion and Cu depletion of CuIn₅Se₈, J. Phys. Chem. C 117 (2013) 10892–10900, https://doi.org/10.1021/jp312467f.

[21] E. Ghorbani, J. Kiss, H. Mirhosseini, G. Roma, M. Schmidt, J. Windeln, T.D. Kühne, C. Felser, Hybrid-functional calculations on the incorporation of Na and K impurities into the CuInSe₂ and CuIn₅Se₈ solar-cell materials, J. Phys. Chem. C 119 (2015) 25197–25203, https://doi.org/10.1021/acs.jpcc.5b07639.

[22] M. Gloeckler, A.L. Fahrenbruch, J.R. Sites, Numerical modeling of CIGS and CdTe solar cells: setting the baseline, in: 3rd World Conf. Photovolt. Energy Convers., Osaka, Japan, 2003, pp. 491–494.

[23] P. Jackson, D. Hariskos, E. Lotter, S. Paetel, R. Wuerz, R. Menner, W. Wischmann, M. Powalla, New world record efficiency for Cu(In,Ga)Se₂ thin-film solar cells beyond 20, Prog. Photovoltaics Res. Appl. 19 (2011) 894–897, https://doi.org/10.1002/pip.1078.

[24] P. Jackson, D. Hariskos, R. Wuerz, W. Wischmann, M. Powalla, Compositional investigation of potassium doped Cu(In,Ga)Se₂ solar cells with efficiencies up to 20.8, Phys. Status Solidi Rapid Res. Lett. 8 (2014) 219–222, https://doi.org/10.1002/pssr.201409040.

[25] P. Jackson, R. Wuerz, D. Hariskos, E. Lotter, W. Witte, M. Powalla, Effects of heavy alkali elements in Cu(In,Ga)Se₂ solar cells with efficiencies up to 22.6, Phys. Status Solidi Rapid Res. Lett. 10 (2016) 583–586, https://doi.org/10.1002/pssr.201600199.

[26] T. Kato, J.L. Wu, Y. Hirai, H. Sugimoto, V. Bermudez, Record efficiency for thin-film polycrystalline solar cells up to 22.9% achieved by Cs-treated Cu(in,Ga)(Se,S)₂, IEEE J. Photovoltaics 9 (2019) 325–330, https://doi.org/10.1109/JPHOTOV.2018.2882206.

[27] T.S. Lopes, J. De Wild, C. Rocha, A. Violas, J.M.V. Cunha, J.P. Teixeira, M. A. Curado, A. Oliveira, J. Borme, G. Birant, G. Brammertz, P.A. Fernandes, B. Vermang, P.M.P. Salomé, On the importance of joint mitigation strategies for front, bulk, and rear recombination in ultrathin Cu(In,Ga)Se₂ solar cells, ACS Appl. Mater. Interfaces 13 (2021) 27713–27725, https://doi.org/10.1021/acsami.1c07943.

[28] J.M.V. Cunha, K. Oliveira, J. Lontchi, T.S. Lopes, M.A. Curado, J.R.S. Barbosa, C. Vinhais, W. Chen, J. Borme, H. Fonseca, J. Gaspar, D. Flandre, M. Edoff, A. G. Silva, J.P. Teixeira, P.A. Fernandes, P.M.P. Salomé, High-performance and industrially viable nanostructured SiOₓ layers for interface passivation in thin film solar cells, Sol. RRL 5 (2021) 2000534, https://doi.org/10.1002/solr.202000534.

[29] A.J.N. Oliveira, J. De Wild, K. Oliveira, B.A. Valença, J.P. Teixeira, J.R. L. Guerreiro, S. Abalde-Cela, T.S. Lopes, R.M. Ribeiro, J.M.V. Cunha, M.A. Curado, M. Monteiro, A. Violas, A.G. Silva, M. Prado, P.A. Fernandes, B. Vermang, P.M. P. Salomé, Encapsulation of nanostructures in a dielectric matrix providing optical enhancement in ultra-thin solar cells, Sol. RRL 4 (2020) 2000310, https://doi.org/10.1002/solr.202000310.

[30] T.S. Lopes, J.M.V. Cunha, S. Bose, J.R.S. Barbosa, J. Borme, O. Donzel-gargand, C. Rocha, R. Silva, A. Hultqvist, W. Chen, A.G. Silva, M. Edoff, P.A. Fernandes, P. M.P. Salomé, Rear optical reflection and passivation using a nanopatterned metal/ dielectric structure in thin-film solar cells, J. Photovoltaics. 9 (2019) 1421–1427, https://doi.org/10.1109/JPHOTOV.2019.2922323.

[31] A.J.N. Oliveira, J.R.S. Barbosa, A. Violas, J.P. Teixeira, K. Oliveira, T. Lopes, J.M. V. Cunha, M.A. Curado, M. Monteiro, C. Rocha, C. Vinhais, P.A. Fernandes, P.M. P. Salomé, Optoelectronic simulations for novel light management concepts in Cu (In,Ga)Se₂ solar cells, in: Physics, Simulation, Photonic Eng. Photovolt. Devices X, 2021, 1168108, https://doi.org/10.1117/12.2577650.

[32] A.J.N. Oliveira, J.P. Teixeira, D. Ramos, P.A. Fernandes, P.M.P. Salomé, Exploiting the optical limits of thin film solar cells: a review on light management strategies in Cu(in,Ga)Se₂, Adv. Photonics Res. (2022), 2100190, https://doi.org/10.1002/adpr.202100190.

[33] P.M.P. Salomé, B. Vermang, R. Ribeiro-andrade, J.P. Teixeira, J.M.V. Cunha, M. J. Mendes, S. Haque, J. Borme, H. Águas, E. Fortunato, R. Martins, J.C. González, J. P. Leitão, P.A. Fernandes, M. Edoff, S. Sadewasser, Passivation of interfaces in thin film solar cells: understanding the effects of a nanostructured rear point contact layer, Adv. Mater. Interfac. 5 (2018), 1701101, https://doi.org/10.1002/admi.201701101.

[34] J.M.V. Cunha, P.A. Fernandes, A. Hultqvist, J.P. Teixeira, S. Bose, B. Vermang, S. Garud, D. Buldu, J. Gaspar, M. Edoff, J.P. Leitao, P.M.P. Salome, Insulator materials for interface passivation of Cu(in,Ga)Se₂ thin films, IEEE J. Photovoltaics 8 (2018) 1313–1319, https://doi.org/10.1109/JPHOTOV.2018.2846674.

[35] C. Van Lare, G. Yin, A. Polman, M. Schmid, Light coupling and trapping in ultrathin Cu(in,Ga)Se₂ solar cells using dielectric scattering patterns, ACS Nano 9 (2015) 9603–9613, https://doi.org/10.1021/acsnano.5b04091.

[36] J.M.V. Cunha, T.S. Lopes, S. Bose, A. Hultqvist, W.C. Chen, O. Donzel Gargand, R. M. Ribeiro, A.J.N. Oliveira, M. Edoff, P.A. Fernandes, P.M.P. Salome, Decoupling of optical and electrical properties of rear contact CIGS solar cells, IEEE J. Photovoltaics (2019) 1–6, https://doi.org/10.1109/jphotov.2019.2933357.

[37] G. Yin, A. Steigert, P. Andrae, M. Goebelt, M. Latzel, P. Manley, I. Lauermann, S. Christiansen, M. Schmid, Integration of plasmonic Ag nanoparticles as a back reflector in ultra-thin Cu(In,Ga)Se₂ solar cells, Appl. Surf. Sci. 355 (2015) 800–804, https://doi.org/10.1016/j.apsusc.2015.07.195.

[38] J. Goffard, C. Colin, F. Mollica, A. Cattoni, C. Sauvan, P. Lalanne, J.-F. Guillemoles, N. Naghavi, S. Collin, Light trapping in ultrathin CIGS solar cells with nanostructured back mirrors, IEEE J. Photovoltaics 7 (2017) 1433–1441, https://doi.org/10.1109/JPHOTOV.2017.2726566.

[39] W.W. Hsu, J.Y. Chen, T.H. Cheng, S.C. Lu, W.S. Ho, Y.Y. Chen, Y.J. Chien, C.W. Liu, Surface passivation of Cu(In,Ga)Se₂ using atomic layer deposited Al₂O₃, Appl. Phys. Lett. 100 (2012), 023508, https://doi.org/10.1063/1.3675849.

[40] R. Kotipalli, B. Vermang, J. Joel, R. Rajkumar, M. Edoff, D. Flandre, Investigating the electronic properties of Al₂O₃/Cu(In,Ga)Se₂ interface, AIP Adv. 5 (2015), 107101, https://doi.org/10.1063/1.4932512.

[41] Lumerical inc., nanophotonic FDTD simulation software - lumerical FDTD (n.d.), https://www.lumerical.com/products/fdtd/. (Accessed 24 November 2020).

[42] T. Kodalle, T. Bertram, R. Schlatmann, C.A. Kaufmann, Effectiveness of an RbF post deposition treatment of CIGS solar cells in dependence of the Cu content of the absorber layer, IEEE J. Photovoltaics 9 (2019) 1839–1845, https://doi.org/10.1109/JPHOTOV.2019.2929418.

[43] R. Kotipalli, O. Poncelet, G. Li, Y. Zeng, L.A. Francis, B. Vermang, D. Flandre, Addressing the impact of rear surface passivation mechanisms on ultra-thin Cu(In, Ga)Se₂ solar cell performances using SCAPS 1-D model, Sol. Energy 157 (2017) 603–613, https://doi.org/10.1016/j.solener.2017.08.055.

[44] Y. Aida, V. Depredurand, J.K. Larsen, H. Arai, D. Tanaka, M. Kurihara, S. Siebentritt, Cu-rich CuInSe₂ solar cells with a Cu-poor surface, Prog. Photovoltaics Res. Appl. 23 (2015) 754–764, https://doi.org/10.1002/pip.2493.

[45] M. Morkel, L. Weinhardt, B. Lohmüller, C. Heske, E. Umbach, W. Riedl, S. Zweigart, F. Karg, Flat conduction-band alignment at the CdS/CuInSe₂ thin-film solar-cell heterojunction, Appl. Phys. Lett. 79 (2001) 4482–4484, https://doi.org/10.1063/1.1428408.

[46] T. Nishimura, H. Sugiura, K. Nakada, A. Yamada, Characterization of interface between accurately controlled Cu-deficient layer and Cu(in,Ga)Se₂ absorber for Cu (in,Ga)Se₂ solar cells, Phys. Status Solidi Rapid Res. Lett. 12 (2018), 1800129, https://doi.org/10.1002/pssr.201800129.

[47] J. Song, S.S. Li, C.H. Huang, O.D. Crisalle, T.J. Anderson, Device modeling and simulation of the performance of Cu(In₁₋ₓ,Gaₓ)Se₂ solar cells, Solid State Electron. 48 (2004) 73–79, https://doi.org/10.1016/S0038-1101(03)00289-2.

[48] Y. Wang, T. Muryobayashi, K. Nakada, Z. Li, A. Yamada, Correlation between carrier recombination and valence band offset effect of graded Cu(In,Ga)Se₂ solar cells, Sol. Energy Mater. Sol. Cells 201 (2019), 110070, https://doi.org/10.1016/j.solmat.2019.110070.

[49] T. Nishimura, S. Toki, H. Sugiura, K. Nakada, A. Yamada, Effect of Cu-deficient layer formation in Cu(In,Ga)Se₂ solar-cell performance, Prog. Photovoltaics Res. Appl. 26 (2018) 291–302, https://doi.org/10.1002/pip.2972.

[50] A. Chirilă, P. Reinhard, F. Pianezzi, P. Bloesch, A.R. Uhl, C. Fella, L. Kranz, D. Keller, C. Gretener, H. Hagendorfer, D. Jaeger, R. Erni, S. Nishiwaki, S. Buecheler, A.N. Tiwari, Potassium-induced surface modification of Cu(In,Ga)Se₂ thin films for high-efficiency solar cells, Nat. Mater. 12 (2013) 1107–1111, https://doi.org/10.1038/nmat3789.

[51] S. Minoura, K. Kodera, T. Maekawa, K. Miyazaki, S. Niki, H. Fujiwara, Dielectric function of Cu(In, Ga)Se₂-based polycrystalline materials, J. Appl. Phys. 113 (2013), 063505, https://doi.org/10.1063/1.4790174.

[52] AIST, AIST PV Technologies: e-ARC (n.d.), https://unit.aist.go.jp/rpd-envene/PV/en/service/e-ARC_en/index_en.html. (Accessed 3 April 2021).

[53] R. Carron, E. Avancini, T. Feurer, B. Bissig, P.A. Losio, R. Figi, C. Schreiner, M. Bürki, E. Bourgeois, Z. Remes, M. Nesladek, S. Buecheler, A.N. Tiwari, Refractive indices of layers and optical simulations of Cu(In,Ga)Se₂ solar cells, Sci. Technol. Adv. Mater. 19 (2018) 396–410, https://doi.org/10.1080/14686996.2018.1458579.

[54] S. Kumar, V. Gupte, K. Sreenivas, Structural and optical properties of magnetron sputtered MgₓZn₁₋ₓO thin films, J. Phys. Condens. Matter 18 (2006) 3343–3354, https://doi.org/10.1088/0953-8984/18/13/002.

[55] P.M.P. Salomé, V. Fjällström, P. Szaniawski, J.P. Leitão, A. Hultqvist, P. A. Fernandes, J.P. Teixeira, B.P. Falcão, U. Zimmermann, A.F. da Cunha, M. Edoff, A comparison between thin film solar cells made from co-evaporated CuIn₁₋ₓGaₓSe₂ using a one-stage process versus a three-stage process, Prog. Photovoltaics Res. Appl. 23 (2015) 470–478, https://doi.org/10.1002/pip.2453.

[56] S.H. Wei, S.B. Zhang, A. Zunger, Effects of Ga addition to CuInSe₂ on its electronic, structural, and defect properties, Appl. Phys. Lett. 72 (1998) 3199–3201, https://doi.org/10.1063/1.121548.

[57] C. Frisk, C. Platzer-Björkman, J. Olsson, P. Szaniawski, J.T. Wätjen, V. Fjällström, P. Salomé, M. Edoff, Optimizing Ga-profiles for highly efficient Cu(In,Ga)Se₂ thin film solar cells in simple and complex defect models, J. Phys. D Appl. Phys. 47 (2014), 485104, https://doi.org/10.1088/0022-3727/47/48/485104.

[58] J. Gong, Y. Kong, J. Li, K. Wang, X. Wang, Z. Zhang, Z. Ding, X. Xiao, Enhancing photocurrent of Cu(In,Ga)Se₂ solar cells with actively controlled Ga grading in the absorber layer, Nano Energy 62 (2019) 205–211, https://doi.org/10.1016/j.nanoen.2019.05.052.

[59] K.F. Tai, R. Kamada, T. Yagioka, T. Kato, H. Sugimoto, From 20.9 to 22.3% Cu(In, Ga)(S,Se) 2 solar cell: reduced recombination rate at the heterojunction and the depletion region due to K-treatment, Jpn. J. Appl. Phys. 56 (2017), 08MC03, https://doi.org/10.7567/JJAP.56.08MC03.

[60] M. Turcu, U. Rau, Recombination mechanisms in Cu(in,Ga)(Se,S)₂ solar cells, in: S. Siebentritt, U. Rau (Eds.), Wide-Gap Chalcopyrites, first ed., Springer, 2006, pp. 102–108.

[61] J. Chen, J. Li, D. Sainju, K.D. Wells, N.J. Podraza, R.W. Collins, MULTILAYER ANALYSIS OF THE CdTe SOLAR CELL STRUCTURE BY SPECTROSCOPIC ELLIPSOMETRY, in: 2006 IEEE 4th World Conf. Photovolt. Energy Conf.,, 2006, pp. 475–478, https://doi.org/10.1109/WCPEC.2006.279494.

[62] S.-H. Wei, A. Zunger, Band offsets at the CdS/CuInSe₂ heterojunction, Appl. Phys. Lett. 63 (1993) 2549–2551, https://doi.org/10.1063/1.110429.

[63] T. Minemoto, T. Matsui, H. Takakura, Y. Hamakawa, T. Negami, Y. Hashimoto, T. Uenoyama, M. Kitagawa, Theoretical analysis of the effect of conduction band offset of window/CIS layers on performance of CIS solar cells using device simulation, Sol. Energy Mater. Sol. Cells 67 (2001) 83–88, https://doi.org/10.1016/S0927-0248(00)00266-X.

[64] H.J. Möller, E.M. Rodak, Investigation of the defect chemistry of CuInSe₂ single crystals by DLTS measurements, in: A. Luque, G. Sala, W. Palz, G. Dos Santos, P. Helm (Eds.), Tenth E.C. Photovolt. Sol. Energy Conf., Kluwer Academic, Boston, 1991, pp. 913–916, https://doi.org/10.1007/978-94-011-3622-8.

[65] A.L. Li, I. Shih, Majority and minority carrier traps in monocrystalline CuInSe₂, J. Electron. Mater. 22 (1993) 195–199, https://doi.org/10.1007/BF02665026.

[66] S. Chatraphorn, K. Yoodee, P. Songpongs, C. Chityuttakan, K. Sayavong, S. Wongmanerod, P.O. Holtz, Photoluminescence of a high quality CuInSe₂ single crystal, Jpn. J. Appl. Phys. 37 (1998) L269–L271, https://doi.org/10.1143/jjap.37.l269.

[67] A.M. Bakry, A.M. Elnaggar, Study of deep levels in Schottky/CuInSe₂ single-crystal devices by deep-level transient spectroscopy measurements, J. Mater. Sci. Mater. Electron. 7 (1996) 191–192, https://doi.org/10.1007/bf00133114.

[68] S.H. Wei, S.B. Zhang, Defect properties of CuInSe₂ and CuGaSe₂, J. Phys. Chem. Solid. 66 (2005) 1994–1999, https://doi.org/10.1016/j.jpcs.2005.10.003.

[69] K. Taretto, U. Rau, Numerical simulation of carrier collection and recombination at grain boundaries in Cu(In,Ga)Se₂ solar cells, J. Appl. Phys. 103 (2008), https://doi.org/10.1063/1.2917293.

[70] M. Gloeckler, J.R. Sites, W.K. Metzger, Grain-boundary recombination in Cu(In,Ga) Se₂ solar cells, J. Appl. Phys. 98 (2005), 113704, https://doi.org/10.1063/1.2133906.

[71] S. Siebentritt, S. Schuler, Defects and transport in the wide gap chalcopyrite CuGaSe₂, J. Phys. Chem. Solid. 64 (2003) 1621–1626, https://doi.org/10.1016/S0022-3697(03)00150-1.

[72] S. Sadewasser, T. Glatzel, S. Schuler, S. Nishiwaki, R. Kaigawa, M.C. Lux-Steiner, Kelvin probe force microscopy for the nano scale characterization of chalcopyrite solar cell materials and devices, 431–432, Thin Solid Films (2003) 257–261, https://doi.org/10.1016/S0040-6090(03)00267-0.

[73] G. Hanna, T. Glatzel, S. Sadewasser, N. Ott, H.P. Strunk, U. Rau, J.H. Werner, Texture and electronic activity of grain boundaries in Cu(In,Ga)Se₂ thin films, Appl. Phys. Mater. Sci. Process 82 (2006) 1–7, https://doi.org/10.1007/s00339-005-3411-1.

[74] P.M.P. Salomé, A. Hultqvist, V. Fjällström, M. Edoff, B. Aitken, K. Vaidyanathan, K. Zhang, K. Fuller, C. Kosik Williams, Cu(In,Ga)Se₂ solar cells with varying Na content prepared on nominally alkali-free glass substrates, IEEE J. Photovoltaics 3 (2013) 852–858, https://doi.org/10.1109/JPHOTOV.2013.2247655.

[75] M.A. Contreras, B. Egaas, K. Ramanathan, J. Hiltner, A. Swartzlander, F. Hasoon, R. Noufi, Progress toward 20% efficiency in Cu(In,Ga)Se₂ polycrystalline thin-film solar cells, Prog. Photovoltaics Res. Appl. 7 (1999) 311–316, https://doi.org/10.1002/(SICI)1099-159X(199907/08)7:4<311::AID-PIP274>3.0.CO;2-G.

[76] M. Powalla, P. Witte, P. Jackson, S. Paetel, E. Lotter, R. Wuerz, F. Kessler, C. Tschamber, W. Hempel, D. Hariskos, R. Menner, A. Bauer, S. Spiering, E. Ahlswede, T.M. Friedlmeier, D. Blázquez-Sánchez, I. Klugius, W. Wischmann, CIGS cells and modules with high efficiency on glass and flexible substrates, IEEE J.

Photovoltaics 4 (2014) 440–446, https://doi.org/10.1109/JPHOTOV.2013.2280468.

[77] L.M. Mansfield, R.L. Garris, K.D. Counts, J.R. Sites, C.P. Thompson, W. N. Shafarman, K. Ramanathan, Comparison of CIGS solar cells made with different structures and fabrication techniques, IEEE J. Photovoltaics 7 (2017) 286–293, https://doi.org/10.1109/JPHOTOV.2016.2616188.

[78] A. Laemmle, R. Wuerz, M. Powalla, Efficiency enhancement of Cu(In,Ga)Se2 thin-film solar cells by a post-deposition treatment with potassium fluoride, Phys. Status Solidi Rapid Res. Lett. 7 (2013) 631–634, https://doi.org/10.1002/pssr.201307238.

[79] C.P. Muzzillo, Review of grain interior, grain boundary, and interface effects of K in CIGS solar cells: mechanisms for performance enhancement, Sol. Energy Mater. Sol. Cells 172 (2017) 18–24, https://doi.org/10.1016/j.solmat.2017.07.006.

[80] S. Siebentritt, E. Avancini, M. Bär, J. Bombsch, E. Bourgeois, S. Buecheler, R. Carron, C. Castro, S. Duguay, R. Félix, E. Handick, D. Hariskos, V. Havu, P. Jackson, H.P. Komsa, T. Kunze, M. Malitckaya, R. Menozzi, M. Nesladek, N. Nicoara, M. Puska, M. Raghuwanshi, P. Pareige, S. Sadewasser, G. Sozzi, A. N. Tiwari, S. Ueda, A. Vilalta-Clemente, T.P. Weiss, F. Werner, R.G. Wilks, W. Witte, M.H. Wolter, Heavy alkali treatment of Cu(in,Ga)Se$_2$ solar cells: surface versus bulk effects, Adv. Energy Mater. 10 (2020), 1903752, https://doi.org/10.1002/aenm.201903752.

[81] N. Nicoara, R. Manaligod, P. Jackson, D. Hariskos, W. Witte, G. Sozzi, R. Menozzi, S. Sadewasser, Direct evidence for grain boundary passivation in Cu(In,Ga)Se$_2$ solar cells through alkali-fluoride post-deposition treatments, Nat. Commun. 10 (2019) 1–8, https://doi.org/10.1038/s41467-019-11996-y.

[82] I.M. Dharmadasa, Fermi level pinning and effects on CuInGaSe$_2$-based thin-film solar cells, Semicond. Sci. Technol. 24 (2009), 055016, https://doi.org/10.1088/0268-1242/24/5/055016.

[83] T. Wada, N. Kohara, S. Nishiwaki, T. Negami, Characterization of the Cu(In,Ga) Se$_2$/Mo interface in CIGS solar cells, Thin Solid Films 387 (2001) 118–122, https://doi.org/10.1016/S0040-6090(00)01846-0.

[84] P. Jackson, R. Würz, U. Rau, J. Mattheis, M. Kurth, T. Schlötzer, G. Bilger, J. H. Werner, High quality baseline for high efficiency, Cu(In$_{1-x}$,Ga$_x$)Se$_2$ solar cells, Prog. Photovoltaics Res. Appl. 15 (2007) 507–519, https://doi.org/10.1002/pip.757.

[85] L.M. Mansfield, A. Kanevce, S.P. Harvey, K. Bowers, C. Beall, S. Glynn, I.L. Repins, Efficiency increased to 15.2% for ultra-thin Cu(In,Ga)Se$_2$ solar cells, Prog. Photovoltaics Res. Appl. 26 (2018) 949–954, https://doi.org/10.1002/pip.3033.

[86] M.A. Contreras, M.J. Romero, B. To, F. Hasoon, R. Noufi, S. Ward, K. Ramanathan, Optimization of CBD CdS process in high-efficiency Cu(In,Ga)Se2-based solar cells, Thin Solid Films. https://doi.org/10.1016/S0040-6090(01)01538-3, 2002, 403-404, 204-211.

[87] M.A. Contreras, J. Tuttle, A. Gabor, A. Tennant, K. Ramanathan, S. Asher, A. Franz, J. Keane, L. Wang, J. Scofield, R. Noufi, HIGH EFFICIENCY Cu(In,Ga)Se$_2$-BASED SOLAR CELLS: processing OF novel absorber structures, in: IEEE 1st World Conf. Photovolt. Energy Convers. - WCPEC (A Jt. Conf. PVSC, PVSEC PSEC), 1994, pp. 68–75, https://doi.org/10.1109/WCPEC.1994.519811.

[88] J. Kessler, C. Chityuttakan, J. Lu, J. Schöldström, L. Stolt, Cu(In,Ga)Se$_2$ thin films grown with a Cu-poor/rich/poor sequence: growth model and structural considerations, Prog. Photovoltaics Res. Appl. 11 (2003) 319–331, https://doi.org/10.1002/pip.495.

[89] P. Jackson, D. Hariskos, R. Wuerz, O. Kiowski, A. Bauer, T.M. Friedlmeier, M. Powalla, Properties of Cu(In,Ga)Se$_2$ solar cells with new record efficiencies up to 21.7, Phys. Status Solidi Rapid Res. Lett. 9 (2015) 28–31, https://doi.org/10.1002/pssr.201409520.

[90] L. Gouillart, W.C. Chen, A. Cattoni, J. Goffard, L. Riekehr, J. Keller, M. Jubault, N. Naghavi, M. Edoff, S. Collin, Reflective back contacts for ultrathin Cu(in,Ga)Se$_2$-based solar cells, IEEE J. Photovoltaics 10 (2020) 250–254, https://doi.org/10.1109/JPHOTOV.2019.2945196.

[91] R. Brendel, H.J. Queisser, On the thickness dependence of open circuit voltages of p-n junction solar cells, Sol. Energy Mater. Sol. Cells 29 (1993) 397–401, https://doi.org/10.1016/0927-0248(93)90098-N.

[92] B. Vermang, V. Fjällström, J. Pettersson, P. Salomé, M. Edoff, Development of rear surface passivated Cu(In,Ga)Se$_2$ thin film solar cells with nano-sized local rear point contacts, Sol. Energy Mater. Sol. Cells 117 (2013) 505–511, https://doi.org/10.1016/j.solmat.2013.07.025.

[93] B. Vermang, J.T. Watjen, C. Frisk, V. Fjallstrom, F. Rostvall, M. Edoff, P. Salome, J. Borme, N. Nicoara, S. Sadewasser, Introduction of Si PERC rear contacting design to boost efficiency of Cu(In,Ga)Se$_2$ solar cells, IEEE J. Photovoltaics 4 (2014) 1644–1649, https://doi.org/10.1109/JPHOTOV.2014.2350696.

[94] A. Hultqvist, T. Sone, S.F. Bent, Buffer layer point contacts for CIGS solar cells using nanosphere lithography and atomic layer deposition, IEEE J. Photovoltaics 7 (2017) 322–328, https://doi.org/10.1109/JPHOTOV.2016.2627621.